Shape Evolution and Single Particle Luminescence of Organometal Halide Perovskite Nanocrystals

Feng Zhu,[†] Long Men,[†,‡] Yijun Guo,[†] Qiaochu Zhu,[†] Ujjal Bhattacharjee,[†,‡] Peter M. Goodwin,[§] Jacob W. Petrich,[*,†,‡] Emily A. Smith,[*,†,‡] and Javier Vela[*,†,‡]

[†]Department of Chemistry, Iowa State University, Ames, Iowa 50011, United States, [‡]U.S. DOE Ames Laboratory, Ames, Iowa 50011, United States, and [§]Center for Integrated Nanotechnologies, Los Alamos National Laboratory, Los Alamos, New Mexico 87545, United States

ABSTRACT Organometallic halide perovskites $CH_3NH_3PbX_3$ (X = I, Br, Cl) have quickly become one of the most promising semiconductors for solar cells, with photovoltaics made of these materials reaching power conversion efficiencies of near 20%. Improving our ability to harness the full potential of organometal halide perovskites will require more controllable syntheses that permit a detailed understanding of their fundamental chemistry and photophysics. In this manuscript, we systematically synthesize $CH_3NH_3PbX_3$ (X = I, Br) nanocrystals with different morphologies (dots, rods, plates or sheets) by using different solvents and capping ligands. $CH_3NH_3PbX_3$ nanowires and nanorods capped with octylammonium halides show relatively higher photoluminescence (PL) quantum yields and long PL lifetimes. $CH_3NH_3PbI_3$ nanowires monitored at the single particle level show shape-correlated PL emission across whole particles, with little photobleaching observed and very few off periods. This work highlights the potential of low-dimensional organometal halide perovskite semiconductors in constructing new porous and nanostructured solar cell architectures, as well as in applying these materials to other fields such as light-emitting devices and single particle imaging and tracking.

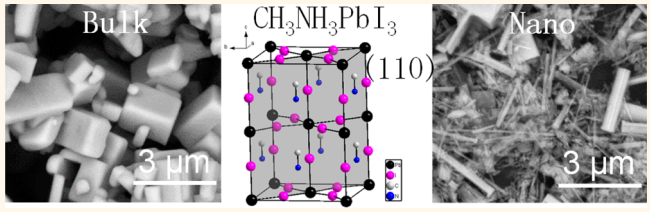

KEYWORDS: organometal halide perovskites · nanocrystals · preferred orientation · morphology control · size control · single particle photoluminescence

Organometal halide perovskites of general composition $CH_3NH_3PbX_3$ ($X^- = Cl^-$, Br^-, I^-) are attractive semiconductor materials due to their low cost and outstanding photovoltaic performance.[1−7] Organometal perovskites can be substituted with a variety of small organic cations and main group metals (in lieu of $CH_3NH_3^+$ and Pb^{2+}, respectively), leading in some cases to improved light harvesting capabilities.[8−14] The organolead perovskites $CH_3NH_3PbBr_3$ and $CH_3NH_3PbI_3$ have bandgaps of 2.3 eV (540 nm) and 1.5 eV (820 nm),[15,16] respectively, as well as high absorption coefficients. Critically, organolead perovskites have very long electron−hole carrier diffusion lengths, exceeding 1 μm in $CH_3NH_3PbI_{3-x}Cl_x$, and 100 nm in $CH_3NH_3PbI_3$, which in principle allows for the development of several solar cell architectures including perovskite-sensitized solar cells, planar heterojunction solar cells, and meso- and nanostructured solar cells.[17] Building on the dramatic improvement of solar cell performance using the solid hole conductor spiro-OMeTAD instead of a liquid electrolyte (spiro-OMeTAD stands for 2,2′-7,7′-tetrakis(*N*,*N*-di-*p*-methoxy-phenylamine)-9,9′-spirobifluorene),[18] the energy conversion efficiency of photovoltaics made from these intensely absorbing, visible-active semiconductors has risen from 3.8% to near 20% in only four years.[19,20]

Photovoltaic performance depends critically on perovskite composition, crystallinity and morphology.[21−23] Higher perovskite film uniformity leads to lower recombination rates in planar heterojuction solar cells.[24,25] Film uniformity is affected by factors such as precursor composition, annealing temperature and, if applicable, solvent used during the vapor-assisted or spin coating deposition process.[6,24,26−32] Highly efficient mesostructured solar cells are produced by a two-step deposition process.[33−35] Vapor-assisted methods and additives provide the means

* Address correspondence to jwp@iastate.edu, esmith1@iastate.edu, vela@iastate.edu.

Received for review December 9, 2014 and accepted February 9, 2015.

Published online February 09, 2015
10.1021/nn507020s

to control the extent of perovskite crystallization.[11,12,36−38] Highly crystalline perovskite domains maximize sunlight harvesting because they have few undesirable grain boundaries, providing well-defined $CH_3NH_3PbI_3$/spiro-OMeTAD interfaces and thus decreasing surface recombination.[26,29,36] Photovoltaic device performance also depends on the relative absence of perovskite bulk defects and surface states.[39−41]

On the basis of their very long electron−hole diffusion lengths (see above), perovskite borne photogenerated carriers should be able to very easily hop across grain boundaries from one single crystalline domain to another, enabling the incorporation of preformed, low-dimensional (nanosized) perovskites into the photoactive layer. Already, some of the best perovskite solar cells reported to date use a photoactive perovskite layer deposited within mesoscopic conductive scaffolds. Nevertheless, preparation methods that could achieve more controllable and favorable crystallinity and morphology are lacking.[47] Development of more complex, advanced solar cell architectures, such as branched solar cells, will require porous perovskite films infiltrated with a transparent charge transporter, which motivates the development of better methods to fabricate and control the composition and morphology of low-dimensional, nanocrystalline perovskites. In addition, small (nanosized) perovskite fluorophores could be of interest outside of the field of photovoltaics, for example in imaging and tracking applications. Highlighting this prospect, $CH_3NH_3PbBr_3$ nanocrystals show relatively high quantum yields of 17%,[42] while crystalline $CH_3NH_3PbI_{3-x}Cl_x$ shows broad PL emission in the biologically relevant near-IR range (albeit, the latter is likely due to surface trap states).[16,43,44]

A few reports describe the synthesis of low dimensional, nanosized organolead halide perovskites. $CH_3NH_3PbI_3$ nanoplatelets were grown on muscovite mica utilizing van der Waals epitaxial growth followed by thermally intercalating methylammonium halides.[45] $CH_3NH_3PbBr_3$ nanocrystals were synthesized using a medium size ammonium bromide-capping agent.[42] $CH_3NH_3PbI_3$ nanocrystals and nanorods were synthesized using solvents with varying polarities or by transformation from PbI_2 crystals.[46,47] While these reports are important developments, the literature on perovskite nanocrystal synthesis remains limited. A more thorough and extensive understanding of the controllable synthesis of different low dimensional lead halide perovskites is desirable. Here, we demonstrate the systematic use of a variety of solvents and capping agents to produce $CH_3NH_3PbI_3$ and $CH_3NH_3PbBr_3$ nanocrystals with different shapes (dot, rod, and plate or sheet morphologies). We also study the optical properties of these differently shaped nanocrystals, and show that dot-, wire-, and sheet-shaped nanocrystals of $CH_3NH_3PbI_3$ display relatively stable and shape correlated photoluminescence at the single particle level.

RESULTS AND DISCUSSION

$CH_3NH_3PbI_3$: Synthesis and Solvent Effects. A simple solution phase method to synthesize organometal perovskites starts by codissolving lead(II)- and methylammonium-halides (PbX_2 and CH_3NH_3X) in a polar solvent such as *N*,*N*-dimethylformamide (ε = 38.25), γ-butyrolactone (ε = 39.1), or acetonitrile (ε = 36.64).[48] An excess of methylammonium halide is often required in order to increase the solubility of lead dihalide, likely due to the formation of a yet unidentified adduct. This mixed precursor solution is then added to a lower polarity solvent such as ethyl acetate (ε = 6.0), chloroform (ε = 4.81) or toluene (ε = 2.38), causing precipitation or "crashing" of crystalline perovskite.

When prepared by the general method above, the dark brown-colored (1.5 eV band gap)[15] perovskite $CH_3NH_3PbI_3$ crystallizes with a tetragonal unit cell (Figure 1).[34−36] Interestingly, the specific combination of precursor (polar) and crashing (nonpolar) solvents has a large effect on the relative diffraction peak intensities observed for this material by XRD (Figure 2). For example, dissolving the methylammonium and lead halide precursors in γ-butyrolactone, followed by crashing with either chlorofom or toluene, yields a product with relatively strong (110) and (220) diffraction peaks and relatively weak (222) and (224) diffraction peaks (Figure 2). This situation indicates preferred orientation and becomes much more dramatic when the precursors are dissolved in acetonitrile, followed by crashing with toluene; in this case, most diffraction peaks become barely visible in comparison to the main (110) and (220) XRD peaks (Figure 2).

$CH_3NH_3PbI_3$: Synthesis and Cation Effects. In a perfectly packed, classical AMX_3 perovskite (where A = cation, M = central cation, and X = anion having ionic radii R_A, R_M, and R_X, respectively), the tolerance factor (t), defined as $t = (R_A + R_X)/\{(\sqrt{2}) \times [R_M + R_X]\}$, must remain close to unity ($t \approx 1$).[49,50] In organometal halide perovskites, only small organic cations consisting of, at most, three C or N atoms are able to fit within the $APbX_3$ structure and fulfill this requirement (for example, when the cation is $CH_3NH_3^+$).[15,51−58] The addition of larger organic cations is expected to either frustrate or terminate the lattice or both, potentially leading to interesting morphology- and size-controlled crystals (for example, nanosized, anisotropic, or layered perovskites).[16] To explore this possibility, we repeated the procedure outlined above while adding a large *n*-octylammonium cation source such as $CH_3(CH_2)_7NH_3I$ and using acetonitrile and toluene as the precursor and crashing solvents, respectively (Scheme 1).

Increasing the initial concentration of $CH_3(CH_2)_7NH_3I$ (z in Scheme 1) in the precursor solution while keeping the concentrations of PbI_2 and CH_3NH_3I constant (x and y,

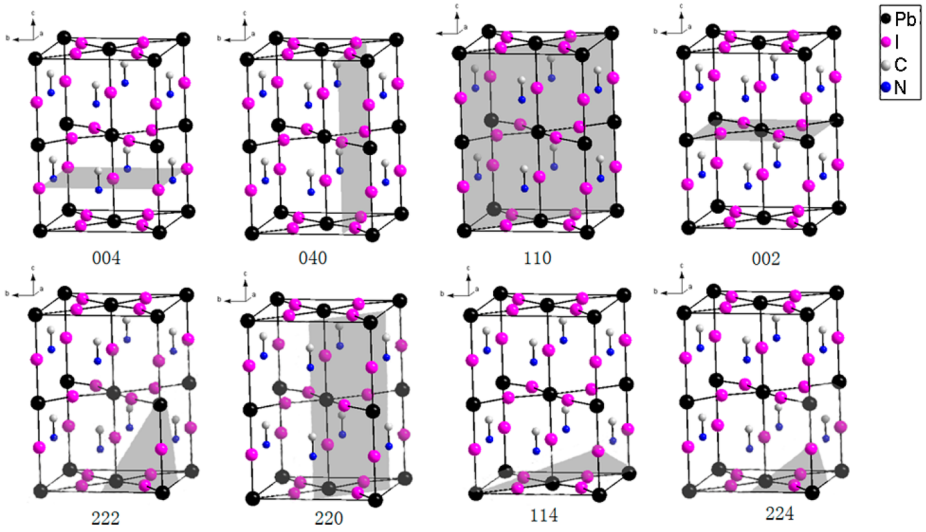

Figure 1. Principal crystallographic (lattice) planes (in gray) for tetragonal $CH_3NH_3PbI_3$.[16]

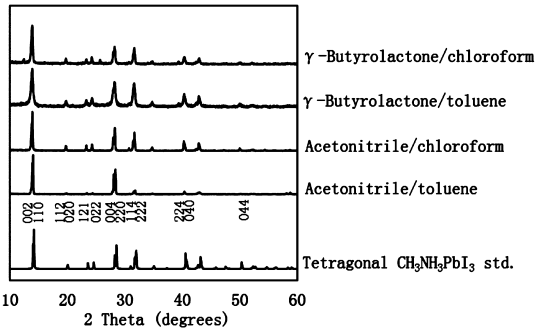

Figure 2. Powder XRD patterns of $CH_3NH_3PbI_3$ samples prepared using different combinations of precursor and crashing solvents. The standard XRD pattern reported for tetragonal $CH_3NH_3PbI_3$ is shown for comparison.

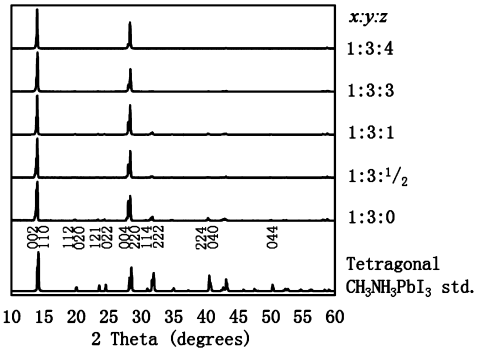

Figure 3. XRD patterns for $CH_3NH_3PbI_3$ prepared using different initial concentrations of PbI_2 (0.435·x mM), CH_3NH_3I (0.435·y mM) and $CH_3(CH_2)_7NH_3I$ (0.435·z mM) in acetonitrile precursor solution and crashed with toluene according to Scheme 1. The standard XRD pattern reported for tetragonal $CH_3NH_3PbI_3$ is shown for comparison.

$$x\ PbI_{2(CH3CN)} + y\ CH_3NH_3I_{(CH3CN)} + z\ n - C_8H_{17}NH_3I_{(CH3CN)} \xrightarrow{\text{Toluene}} CH_3NH_3PbI_{3(s)}$$

Scheme 1

respectively) leads to a progressive increase in the relative intensity of the (110) and (220) XRD diffraction peaks (Figure 3). Similar to what is observed for certain solvents (see above), this strongly indicates that the individual perovskite crystals either pack or grow (*i.e.*, orient) themselves preferentially along the [110] and (related) [220] directions (see below). Critically, none of the other known and related $(CH_3NH_3)_nPbI_m$ (n,m = 2,4; 3,5; 4,6) phases are observed by XRD (see Supporting Information available).

$CH_3NH_3PbI_3$: Preferred Orientation and Direction of Growth. To better understand the microscopic basis for the preferred orientation behavior observed for $CH_3NH_3PbI_3$ by XRD, we performed additional characterization using Scanning and Transmission Electron Microscopies (SEM and TEM). "Bulk" $CH_3NH_3PbI_3$ made in the absence of any directing agents (without $CH_3(CH_2)_7NH_3I$) consists of relatively large 0.3−2 μm particles having cube-like or tetragonal morphology (Figure 4a and Table 1, entry 1). In contrast, $CH_3NH_3PbI_3$ made by reacting acetonitrile solutions of PbI_2, CH_3NH_3I, and $CH_3(CH_2)_7NH_3I$ with toluene consists of high aspect ratio, elongated nanocrystals having wire- and rod-like morphologies (Figure 4, panels b and c, respectively). High-resolution transmission electron microscopy (HR-TEM) shows that the elongated perovskite single crystals grow along the [110] crystallographic direction; in other words, the main (long) axis of these perovskite nanowires and nanorods is perpendicular to the (220) set of lattice planes, which have a d spacing of 3.14 Å (Figure 5).

$CH_3NH_3PbI_3$: Morphology and Aspect Ratio Control. We find that a convenient way of controlling the aspect ratio of $CH_3NH_3PbI_3$ nanorods and nanowires is by fine-tuning the rate at which the precursor solution is added to the crashing solvent. For example, single (fast) addition of an acetonitrile solution (4.6 mL) containing PbI_2 (0.435 mM), CH_3NH_3I (1.305 mM), and $CH_3(CH_2)_7NH_3I$ (1.305 mM) to toluene (15 mL) produces relatively long and thin (1500 nm × 34 nm) $CH_3NH_3PbI_3$ nanowires,

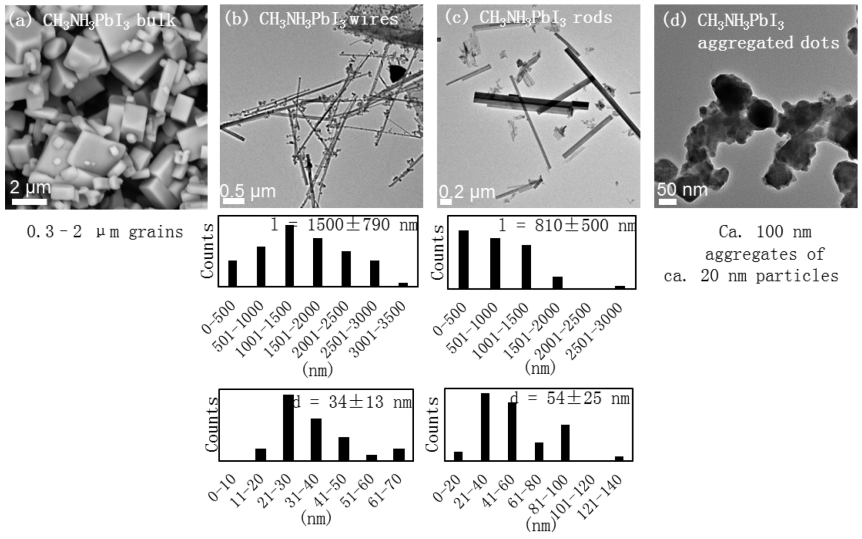

Figure 4. Representative SEM (a) and TEM (b–d) images and size histograms for crystalline $CH_3NH_3PbI_3$ obtained without additional cations or ligands (a), by single (fast) addition (b), or slow addition (0.01 mL/min) (c) of an acetonitrile solution (4.6 mL) containing PbI_2 (0.435 mM), CH_3NH_3I (1.305 mM) and $CH_3(CH_2)_7NH_3I$ (1.305 mM) to toluene (15 mL), and by single (fast) addition of a γ-butyrolactone solution (0.5 mL) containing PbI_2 (2.5 mM), CH_3NH_3I (1.25 mM) and $(H_3NCH_2CH_2CHNH_3CH_2CH_3)I_2$ (1.25 mM) to toluene (15 mL) (d).

TABLE 1. Methylammonium-Lead Iodide and Bromide Perovskites Synthesized under Various Conditions[a]

no.	sample	dimensions	band gap (ev)	PL_{max} (nm)	quantum yield (%)	lifetime (ns)[b]
1	$CH_3NH_3PbI_3$ bulk	0.3–2 μm	1.56	762	0.34	9
2	$CH_3NH_3PbI_3$ wires	1500 nm × 34 nm	1.57	756	1.7	30
3	$CH_3NH_3PbI_3$ rods	810 nm × 54 nm	1.57	760	1.4	66
4	$CH_3NH_3PbI_3$ dots (aggregated)	Dots: 20 nm (Aggregates: 100 nm)	1.62	744	0.025	-[c]
5	$CH_3NH_3PbBr_3$ bulk	200–800 nm	2.26	540	1.2	-[c]
6	$CH_3NH_3PbBr_3$ wires	500 nm ×47 nm	2.30	531	13	-[c]
7	$CH_3NH_3PbBr_3$ plates	150 nm ×30 nm	2.30	520	0.43	-[c]

[a] See Methods for details. [b] Supporting Information for details. [c] Not measured.

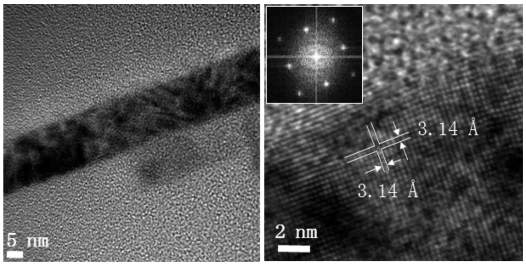

Figure 5. Representative TEM, HRTEM and FFT images of a $CH_3NH_3PbI_3$ nanowire.

along with a minor fraction of smaller (*ca.* 24 nm) $CH_3NH_3PbI_3$ nanocrystals (Figure 4b and Table 1, entry 2). When the precursor solution addition rate is slowed down to 0.01 mL/min, the wires become shorter and fatter (810 nm × 54 nm), with a much-reduced fraction of small nanocrystals formed as a byproduct (Figure 4c and Table 1, entry 3). Critically, only nanocrystals produced in the presence of $CH_3(CH_2)_7NH_3I$ contain a strong asymmetric C–H stretching vibration at 2940–2915 cm^{-1}, consistent with the presence of CH_2-containing C8 groups, likely on the surface of the particles (see Supporting Information). Interestingly, when 1,3-pentanediammonium iodide ($(H_3NCH_2CH_2CHNH_3CH_2CH_3)I_2$) and γ-butyrolactone are used instead of *n*-octyl ammonium iodide and acetonitrile, XRD shows the formation of a crystalline product made up of much smaller single crystalline domains that lack the preferred orientation behavior observed above, as evidenced by the very broad diffraction peaks and the resemblance of their relative intensity compared to the standard XRD pattern, respectively (Figure 6 and Table 1, entry 4). TEM shows that the product of this reaction is composed of aggregates of relatively small (*ca.* 20 nm), isotropic nanodots (Figure 4d). These data suggest that the bidentate nature of the diammonium 1,3-pentanediammonium cation has two effects: First, it behaves as a larger, more sterically encumbered organic dication, leading to more extensive capping and termination and thus to smaller crystalline domains. Second, because this dication has two ammonium headgroups, it can easily link neighboring nanocrystal surfaces, leading to the observed aggregation.

$CH_3NH_3PbBr_3$: Morphology and Aspect Ratio Control. The yellow-colored (2.3 eV band gap)[15,16] $CH_3NH_3PbBr_3$ perovskite crystallizes with a cubic unit cell (Figure 7). On the basis of the aforementioned effects of solvent, cation and precursor addition rate on the synthesis of crystalline $CH_3NH_3PbI_3$, we sought to use a similar approach to control the size and shape of $CH_3NH_3PbBr_3$ nanocrystals. We specifically used lead(II)-, methylammonium-, and *n*-octylammonium-bromide as precursors, and a combination of *N*,*N*-dimethylformamide (DMF) and toluene as the precursor and crashing solvents, respectively (Scheme 2).

The XRD pattern of "bulk" $CH_3NH_3PbBr_3$ obtained in the absence of large cation sources closely resembles the standard pattern reported for cubic $CH_3NH_3PbBr_3$, indicating that there is no preferred orientation in this sample (Figure 8).[17] In contrast, addition of n-$C_8H_{17}NH_3Br$ to the precursor solution during synthesis causes a very significant increase in the relative intensities of the (001) and (002) diffractions in comparison to the rest of the peaks in the standard pattern of this material; this observation strongly indicates that crystalline $CH_3NH_3PbBr_3$ made in this way preferentially grows along the [001] crystallographic direction (Figure 8).

In agreement with our XRD observations, TEM shows that $CH_3NH_3PbBr_3$ made in the absence of large organic cations (without $CH_3(CH_2)_7NH_3Br$) consists of relatively large 0.2−0.8 μm particles (Figure 9a and Table 1, entry 5). In contrast, $CH_3NH_3PbBr_3$ made by reacting DMF solutions of $PbBr_2$, CH_3NH_3Br and $CH_3(CH_2)_7NH_3Br$ with toluene consists of much smaller and higher aspect ratio, anisotropic nanocrystals having wire- and plate-like morphologies (Figure 9, panels b and c, respectively). In this case, a convenient way of controlling the specific morphology of $CH_3NH_3PbBr_3$ nanocrystals is to vary the initial concentration of methyl- and *n*-octyl-ammonium (C1 and C8) bromides

$$x\ PbBr_{2(DMF)} + y\ CH_3NH_3Br_{(DMF)} + z\ n-C_8H_{17}NH_3Br_{(DMF)} \xrightarrow{\text{Toluene}} CH_3NH_3PbBr_{3(s)}$$

Scheme 2

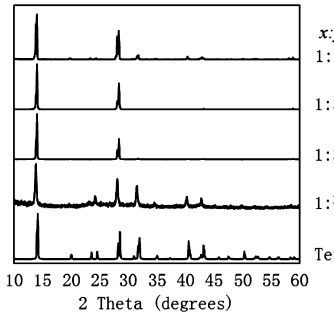

Figure 6. Powder XRD patterns of $CH_3NH_3PbI_3$ obtained by addition of an acetonitrile solution (4.6 mL) containing PbI_2 (0.435·x mM), CH_3NH_3I (0.435·y mM), and $CH_3(CH_2)_7NH_3I$ (0.435·z mM) or a γ-butyrolactone solution (0.5 mL) containing PbI_2 (2.5·x mM), CH_3NH_3I (2.5·y mM) and $(H_3NCH_2CH_2CHNH_3CH_2CH_3)I_2$ (2.5·RN_2I_2 mM) to toluene (15 mL) according to Scheme 1 (unless specified otherwise, the precursor solution was added at once, as a fast, single addition). The standard XRD pattern reported for tetragonal $CH_3NH_3PbI_3$ is shown for comparison.

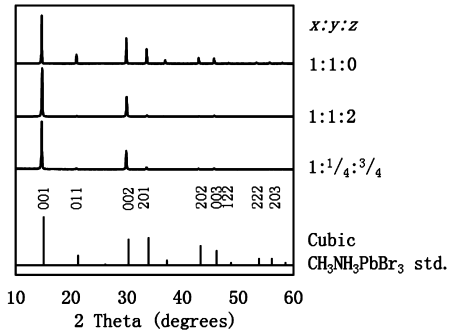

Figure 8. Powder XRD patterns of $CH_3NH_3PbBr_3$ obtained by addition of a DMF solution (1.5 mL) containing $PbBr_2$ (2.7·x mM), CH_3NH_3Br (2.7·y mM) and $CH_3(CH_2)_7NH_3Br$ (2.7·z mM) to toluene (15 mL) according to Scheme 2. The precursor solution was added at once (fast, in a single addition). The standard XRD pattern reported for cubic $CH_3NH_3PbBr_3$ is shown for comparison (generated from literature data using Diamond).[59]

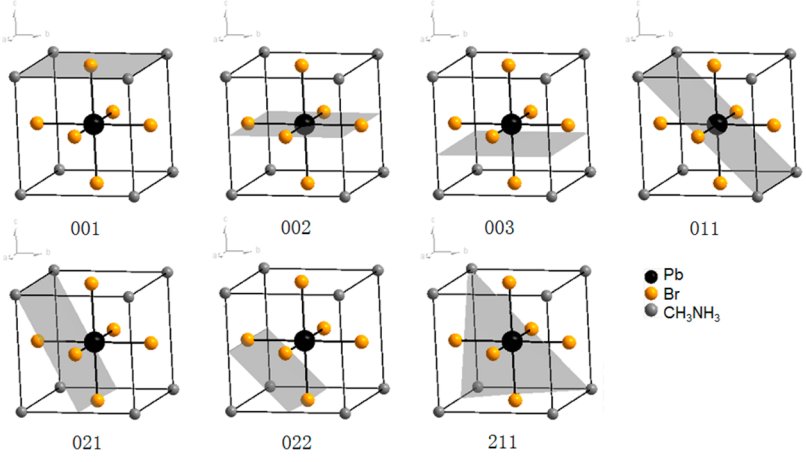

Figure 7. Principal crystallographic (lattice) planes (in gray) for cubic $CH_3NH_3PbBr_3$.[59]

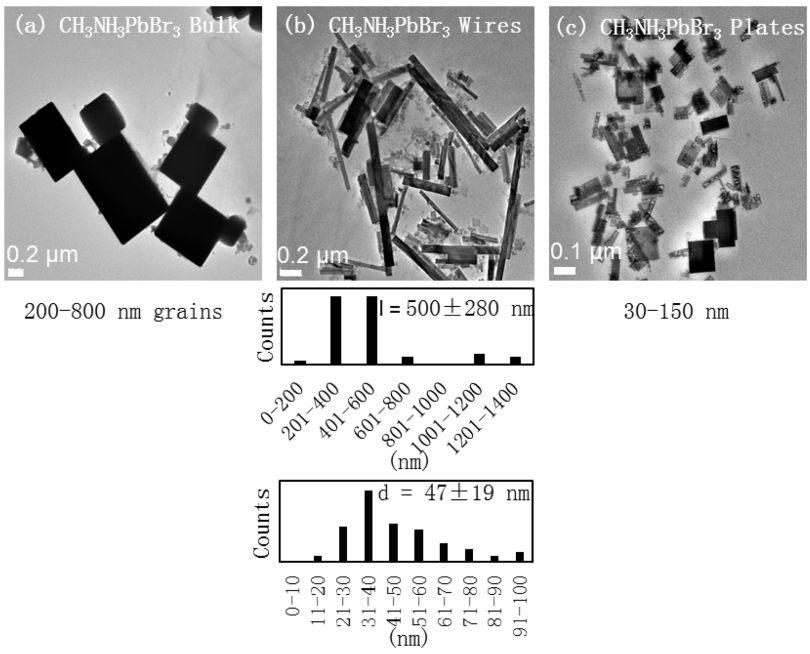

Figure 9. Representative TEM images and size histograms for crystalline $CH_3NH_3PbBr_3$ obtained without additional cations or ligands (a), and by single addition of a DMF solution (1.5 mL) toluene (15 mL) containing $PbBr_2$ (2.7 mM), CH_3NH_3Br (2.7 mM) and $CH_3(CH_2)_7NH_3Br$ (5.4 mM) (b) or $PbBr_2$ (2.7 mM), CH_3NH_3Br (0.68 mM) and $CH_3(CH_2)_7NH_3Br$ (2.0 mM) (c).

in the DMF precursor solution. For example, single addition of a DMF solution (1.5 mL) containing $PbBr_2$ (2.7 mM), CH_3NH_3Br (2.7 mM) and $CH_3(CH_2)_7NH_3Br$ (5.4 mM) to toluene (15 mL) produces $CH_3NH_3PbBr_3$ nanowires (500 nm × 47 nm) (Figure 9b and Table 1, entry 6). When this experiment is repeated with the same $PbBr_2$ concentration (2.7 mM) while decreasing the concentration of CH_3NH_3Br (0.68 mM) and $CH_3(CH_2)_7NH_3Br$ (2.0 mM), the product is made of smaller elongated $CH_3NH_3PbBr_3$ nanocrystals (150 nm × 30 nm) with plate-like morphology (Figure 9b and Table 1, entry 7).

Instability of $CH_3NH_3PbBr_3$ under a TEM Beam. During structural characterization by TEM, we noticed that $CH_3NH_3PbBr_3$ nanocrystals are particularly unstable under an electron beam. For example, when imaging with a FEI-Tecnai 2-F20 STEM operating at 200 kV, $CH_3NH_3PbBr_3$ nanoplates quickly (3−5 min) "melt" away to form smaller dot-like particles of unknown composition (Figure 10). The particles produced in this way were not particularly crystalline, and thus far we were unable to identify their exact composition. This behavior is not unique to nanocrystalline $CH_3NH_3PbBr_3$, as bulk $CH_3NH_3PbBr_3$ decomposed just as fast under the electron beam (see Supporting Information). The close resemblance between this behavior and a recently reported synthesis of $CH_3NH_3PbBr_3$ nanodots raises questions about the true nature of such particles.[42] The thermal stability of perovskites has been explored using thermogravimetric analysis (TGA) and differential scanning calorimetry (DSC).[16,60] For $CH_3NH_3PbI_3$, a transition occurs from tetragonal to cubic phase between 55 and 57 °C. Consecutive HI (20%) and CH_3NH_2 (5−6%)

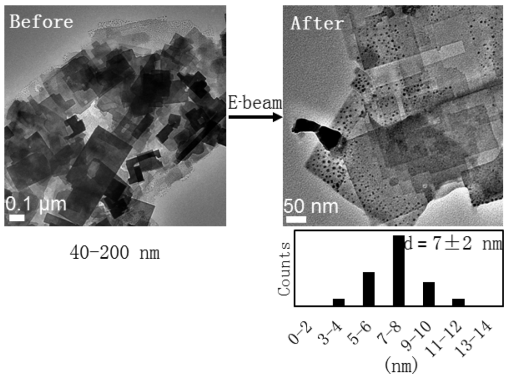

Figure 10. TEM images of $CH_3NH_3PbBr_3$ plates immediately after and a few (3−5) minutes after exposure to the TEM electron beam of a FEI-Tecnai 2-F20 STEM operating at up to 200 kV.

losses are said to occur between 300 and 420 °C. An additional transition between 550 and 600 °C is in good agreement with PbI_2. In contrast to $CH_3NH_3PbBr_3$ however, $CH_3NH_3PbI_3$ did not display any sign of decomposition under the electron beam during TEM characterization.

Ensemble Optical Properties of $CH_3NH_3PbI_3$ and $CH_3NH_3PbBr_3$. Figures 11 and 12 show solid-film diffuse reflectance, solution-phase optical absorption, and photoluminescence spectra of several $CH_3NH_3PbI_3$ and $CH_3NH_3PbI_3$ perovskites, respectively. The diffuse reflectance spectra (Figures 11a and 12a) are particularly helpful in determining the absorption onsets of these materials because, due to partial or incomplete solubility (particularly for large and bulk particles), solution-phase absorption spectra of these materials show a

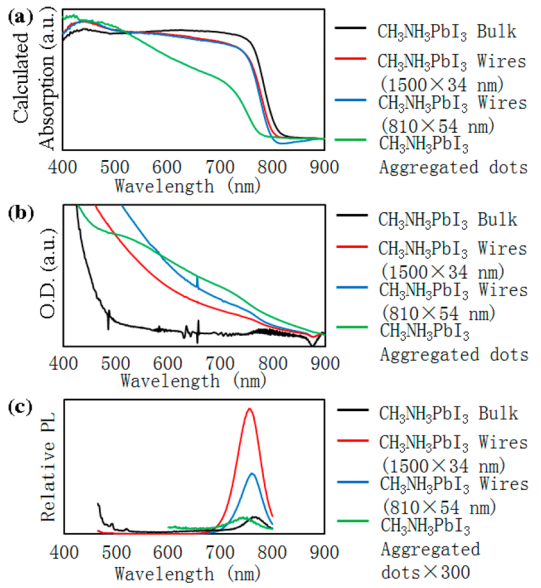

Figure 11. Solid-film diffuse reflectance (a), solution-phase optical density (O.D. includes absorption and scattering) (b), and relative photoluminescence spectra (normalized by each sample's O.D. at λ_{exc} = 450 nm) (c) of $CH_3NH_3PbI_3$ perovskites with different size and morphology (a.u. = arbitrary units).

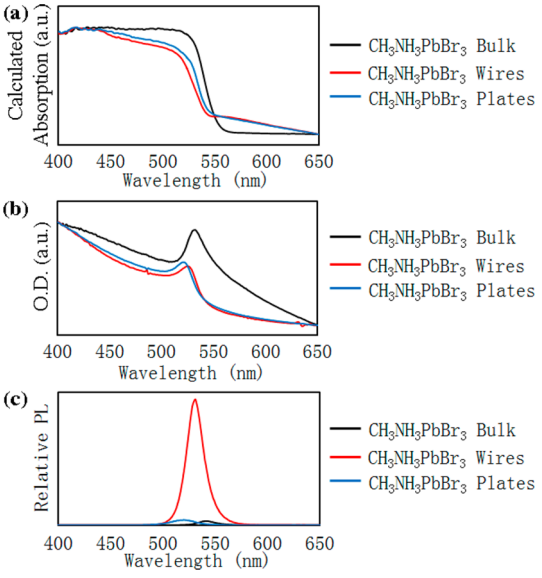

Figure 12. Solid-film diffuse reflectance (a), solution-phase optical density (O.D. includes absorption and scattering) (b), and relative photoluminescence spectra (normalized by each sample's O.D. at λ_{exc} = 350 nm) (c) of $CH_3NH_3PbBr_3$ perovskites with different size and morphology (a.u. = arbitrary units).

significant amount of scattering at photon energies below their band gap (Figures 11b and 12b). Nevertheless, the solution-phase spectra possess features worth noting. A lack of obvious excitonic peaks in the solution-phase absorption spectra of $CH_3NH_3PbI_3$ can be attributed to its exciton binding energy (45 meV) being similar to k_BT at room temperature (25 meV, k_B = Boltzmann constant) (Figure 11b).[52] In contrast, the solution-phase absorption spectra of $CH_3NH_3PbBr_3$ shows clear excitonic peaks for all different morphologies (Figure 12b), in agreement with its higher exciton binding energy (150 eV).[52]

As expected, bulk $CH_3NH_3PbI_3$ and $CH_3NH_3PbBr_3$ samples show absorption onsets of about 800 and 550 nm, respectively (Figures 11a and 12a). The absorption edge remains almost unchanged (<5 nm blue-shift) for $CH_3NH_3PbI_3$ nanowires compared to bulk $CH_3NH_3PbI_3$, but is significantly blue-shifted (by about 30 nm) for the aggregated $CH_3NH_3PbI_3$ dots (Figure 11). In turn, the absorption edge is blue-shifted by about 10 nm for $CH_3NH_3PbBr_3$ wires and plates compared to bulk $CH_3NH_3PbBr_3$ (Figure 12). The specific apparent band gaps, measured from the absorption data using Tauc plots ($(Ah\nu)^2$ *vs* $h\nu$ for a direct band gap semiconductor, where A = absorption coefficient, $h\nu$ = energy of light) were 1.56 eV for bulk $CH_3NH_3PbI_3$, 1.57 eV for $CH_3NH_3PbI_3$ wires, and 1.62 eV for aggregated $CH_3NH_3PbI_3$ dots; 2.26 eV for bulk $CH_3NH_3PbBr_3$, 2.30 eV for $CH_3NH_3PbBr_3$ wires, and 2.30 eV for $CH_3NH_3PbBr_3$ plates. The mechanisms leading to these shifts are presently unknown; however, the shifts do not appear to originate from quantum confinement, because the crystalline domains (as determined by XRD and TEM, Table 1) are larger than the reported Bohr radii (2.2 nm and 2.0 nm for $CH_3NH_3PbI_3$ and $CH_3NH_3PbBr_3$, respectively).[61] It is worth noting that some references have attributed a narrowing in the optical band gap of larger organometal halide perovskite crystals to changes in the degree of Pb−I bond stress.[62]

An interesting characteristic of organometal perovskite semiconductors is that they are good fluorophores and can be highly emissive. Given the ease with which these materials perform photoinduced charge separation in high performance photovoltaics, it could appear counterintuitive that they can perform radiative recombination. However, light emission is often observed in materials used for light-emitting diodes and solar cells, as this indicates that nonradiative relaxation pathways are relatively slow.[63] For example, GaAs and PbS can exhibit high PL quantum yields and high photovoltages in solar cells.[64] In addition, such emission properties may actually be useful in studying the structural and photophysical causes for radiative energy loss in photovoltaic devices, as well as in enabling different applications outside of the solar cell realm, for example in light emitting devices or in single particle imaging and tracking.

Among the different perovskites synthesized here, bulk $CH_3NH_3PbI_3$ and aggregated $CH_3NH_3PbI_3$ dots have low PL quantum yields (QYs) of 0.34% and 0.025%, respectively, indicating that nonradiative exciton decay is dominant in these samples. Because

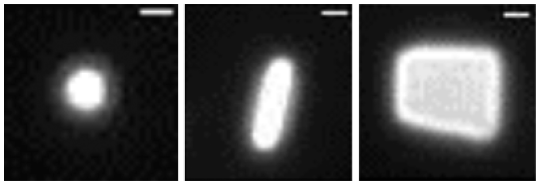

Figure 13. Single particle photoluminescence images obtained from movies of 25 s duration of $CH_3NH_3PbI_3$ nanocrystals with dot-, wire-, and plate-like morphologies (please see Supporting Information Movies S1, S2, and S3, respectively) (λ_{exc} = 540 nm, λ_{PL} = 700 nm, scale bar = 1 μm).

structural defects are known to play a crucial role in perovskite optical properties,[20,65,66] this weak PL intensity could be attributed to surface defects. In agreement with this idea, $CH_3NH_3PbI_3$ wires and rods made in the presence of the surface passivating n-octylammonium cation have a higher PL QYs of 1.7−1.4%, and their PL lifetimes inversely correlate with their aspect and surface-to-volume ratios (Table 1, see also Supporting Information). In comparison to $CH_3NH_3PbI_3$, crystalline $CH_3NH_3PbBr_3$ samples display more intense emission, with PL QYs of 1.2%, 13%, and 0.43% for bulk, wires, and plates, respectively (Table 1).

Single Particle Fluorescence Microscopy: Shape-Correlated Single Particle Emission. To obtain a deeper insight into the photoluminescence behavior of perovskite crystals having different size and morphology, we utilized single particle fluorescence microscopy. To our surprise, different $CH_3NH_3PbI_3$ nanocrystals sustain synchronous photoluminescence at the single particle level under continuous photoexcitation above their band gap (Figure 13). More specifically, wire-, rod-, and dot-like $CH_3NH_3PbI_3$ nanocrystals show shape-correlated photoluminescence emission across whole particles, with little photobleaching or photobrightening observed in some cases, and with few off periods (see Supporting Information). This type of behavior, while precedented, is rare. Synchronous blinking (displaying both on and off photoluminescent periods) spanning the entire length of II−VI (CdSe) semiconductor quantum nanowires with 9 nm diameter and >5 μm length was described and explained by a dynamic, transient photolytic filling of surface-trap sites.[67−73] More typically, 1D nanostructures such as $GaAs/Ga_xIn_{1-x}P$ ($0.34 < x < 0.69$) and GaAs/GaAsP nanowires with <20 nm diameter display low temperature emission from their tips (only from the nanowire ends).[74−83] Here, $CH_3NH_3PbI_3$ nanocrystals with several distinct morphologies behave as nonblinking and photostable single particle emitters at room temperature. These results were corroborated by registered atomic force microscopy-photoluminescence (AFM-PL) experiments, which showed that $CH_3NH_3PbI_3$ nanowires under steady excitation continuously emit along their length (Figure 14). Interestingly, the single particle PL lifetime measured by AFM-PL is *ca.* 40 ns, which is

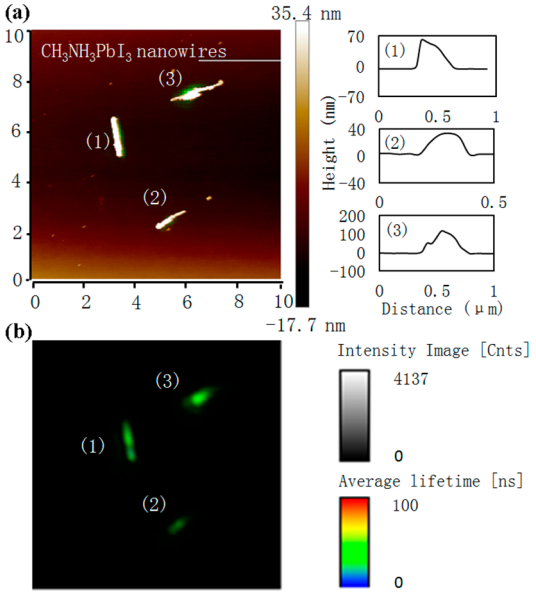

Figure 14. Correlated AFM-PL (a) and PL-only (b) images of $CH_3NH_3PbI_3$ nanowires (λ_{exc} = 485 nm). Nanowire heights were determined from the difference between the particle and background heights.

roughly similar to the ensemble PL lifetime of 30 ns measured for the same $CH_3NH_3PbI_3$ nanowire sample (Figure 14 and Table 1, entry 2).

CONCLUSION

Crystalline $CH_3NH_3PbX_3$ (X = I, Br) particles were synthesized by adding lead(II) halide and methylammonium halide precursor solutions in polar solvents (CH_3CN, γ-butyrolactone, DMF) to a much less polar solvent (toluene, chloroform). $CH_3NH_3PbX_3$ crystals show preferred orientation when the precursors are dissolved in acetonitrile (X = I) or DMF (X = Br), followed by crashing or precipitation with toluene. A similar effect, along with a significant decrease in particle size, is observed when larger or multidentate organic cations such as on *n*-octylammonium and 1,3-pentanediammonium, respectively, are introduced to the synthesis. High-resolution (HR) TEM shows that the observed preferred orientation is due to elongation of the perovskite single nanocrystals along the [110] or [001] crystallographic directions of tetragonal $CH_3NH_3PbI_3$ or cubic $CH_3NH_3PbBr_3$ perovskites, respectively. Varying the initial rate of precursor addition, as well as the initial concentrations of lead(II)-, methyl-, and *n*-octyl-ammonium halides, allows to control the relative aspect ratio of the final nanocrystals (from bulk to wires to rods to dots in the case of $CH_3NH_3PbI_3$, and from bulk to wires to plates or sheets in the case of $CH_3NH_3PbBr_3$). Importantly, $CH_3NH_3PbBr_3$ nanocrystals are particularly unstable under an electron beam, "melting" away to form smaller dot-like particles of unknown composition during TEM analysis.

$CH_3NH_3PbI_3$ nanowires show PL quantum yields between 1.4 and 1.7% depending on their aspect ratio. $CH_3NH_3PbI_3$ wires show lifetimes of 30−60 ns, longer than bulk $CH_3NH_3PbI_3$, which we attribute to better surface passivation by the n-octylammonium cation. $CH_3NH_3PbBr_3$ nanowires show a PL quantum yield of 13%, significantly higher than that of the corresponding $CH_3NH_3PbBr_3$ bulk or aggregated dots. Under single particle fluorescence microscopy, wire-, rod-, and dot-like $CH_3NH_3PbI_3$ nanocrystals show coherent, shape-correlated photoluminescence emission across whole particles, with little photobleaching (or photobrightening) observed and very few off periods. The differently shaped $CH_3NH_3PbI_3$ and $CH_3NH_3PbBr_3$ nanocrystals may be of future use in the construction of porous solar cells, and in the study the effect of morphology and crystallization on solar cell performance.

METHODS

Materials. Lead(II) iodide (99%), lead(II) bromide (≥98%), methylamine solution (33 wt % in absolute ethanol), *N*,*N*-dimethylformamide (DMF, anhydrous, 99.8%), 1,3-pentanediamine (Dytek EP diamine, 98%), γ-butyrolactone (≥99%), *n*-octylamine (99%), and 1-octadecene (tech., 90%) were purchased from Sigma-Aldrich. Hydroiodic acid (ACS, 55−58%), hydrobromic acid (ACS, 47.0−49.0%) and oleic acid (tech., 90%) were from Alfa-Aesar; acetonitrile (99.9%), toluene (99.9%), tetrahydrofuran (THF, 99.0%), and acetone (99.9%) were from Fisher. All chemicals were used as received unless specified otherwise.

Synthesis. *Ammonium Halides.* Hydrogen halides were prepared by a modified literature procedure.[84] Briefly, hydroiodic acid (10 mL, 0.075 mol) or hydrobromic acid (8.6 mL, 0.075 mol) was added to a solution of excess methylamine (24 mL, 0.192 mol) in ethanol (100 mL) at 0 °C, and the mixture stirred for 2 h. The solution was concentrated under vacuum, and the resulting powder was dried under dynamic vacuum at 60 °C for 12 h, then recrystallized from ethanol. *n*-Octylammonium iodide ($CH_3(CH_2)_7NH_3I$), *n*-octylammonium bromide ($CH_3(CH_2)_7NH_3Br$), and 1,3-pentanediammonium iodide were washed repeatedly with ethyl ether and dried under dynamic vacuum before use.

$CH_3NH_3PbI_3$. PbI_2 (9.2 mg, 0.02 mmol) and CH_3NH_3I (3.2 mg, 0.02 mmol) were added into γ-butyrolactone (4 mL). A fraction (0.4 mL) of this solution was dropped into hexane, THF, 1,4-dioxane, acetone, ethyl acetate, chloroform or toluene (15 mL). To study the effect of organic cations, a solution A was made by dissolving PbI_2 (9.2 mg, 0.02 mmol) and CH_3NH_3I (9.6 mg, 0.06 mmol) in acetonitrile (40 mL). Another solution B was made by dissolving $CH_3(CH_2)_7NH_3I$ (10.3 mg, 0.04 mmol) in acetonitrile (4 mL). For bulk $CH_3NH_3PbI_3$, solution A (4 mL) was added to toluene (15 mL) while stirring. For $CH_3NH_3PbI_3$ nanocrystals (nanowires and nanorods), different amounts of solution B were mixed with solution A (4 mL, 0.002 mmol), and the mixture was added into toluene (15 mL). For aggregated $CH_3NH_3PbI_3$ dots, PbI_2 (23.1 mg, 0.05 mmol), CH_3NH_3I (4 mg, 0.025 mmol) and 1,3-pentanediammonium iodide (9 mg, 0.025 mmol) were used.

$CH_3NH_3PbBr_3$. $PbBr_2$ (58.8 mg, 0.16 mmol) was dissolved in DMF (20 mL), CH_3NH_3Br (17.6 mg, 0.16 mmol) in DMF (20 mL), and $CH_3(CH_2)_7NH_3Br$ (16.8 mg, 0.08 mmol) in DMF (5 mL). For bulk $CH_3NH_3PbBr_3$, a mixture of $PbBr_2$ (0.5 mL, 0.004 mmol) and CH_3NH_3Br (0.5 mL, 0.004 mmol) solutions was added to toluene (15 mL) while stirring. For anisotropic $CH_3NH_3PbBr_3$ nanocrystals, a mixture of $PbBr_2$ (0.5 mL, 0.004 mmol), CH_3NH_3Br (0.5 mL, 0.004 mmol for wires; 0.125 mL, 0.001 mmol for plates), and $CH_3(CH_2)_7NH_3Br$ (0.5 mL, 0.008 mmol for wires; 0.188 mL, 0.003 mmol for plates) was added into toluene (15 mL) while stirring. In all cases, samples were allowed to stand for 24 h before isolating the product by centrifugation (10 min at 4000 rpm) and washing with toluene (5 mL).

Structural Characterization. *Powder X-ray Diffraction (XRD).* XRD data were measured using Cu Kα radiation on Rigaku Ultima IV (40 kV, 44 mA). Samples were prepared by drop casting from toluene onto a "background-less" quartz sample holder.

Transmission Electron Microscopy (TEM). TEM was conducted using a FEI Technai G2 F20 field emission TEM operating at up to 200 kV with a point-to-point resolution of less than 0.25 nm and a line-to-line resolution of less than 0.10 nm. Samples were prepared by placing 2 or 3 drops of dilute toluene solutions onto carbon-coated copper grids.

Size and Morphology Analysis. Material dimensions were measured manually or with ImageJ or both. Uncertainties in all measurements are reported as standard deviations.

Optical Characterization. *Optical Extinction.* Optical Extinction (absorption plus scattering) spectra of solutions were measured with a photodiode-array Agilent 8453 UV/vis spectrophotometer. Solvent absorption was recorded and subtracted from all spectra.

Diffuse Reflectance. Diffuse reflectance spectra of solid films were measured with a SL1 Tungsten Halogen lamp (vis-IR), a SL3 Deuterium Lamp (UV), and a BLACK-Comet C-SR-100 Spectrometer. Samples were prepared by drop-casting toluene solutions onto glass.

Steady-State Photoluminescence (PL). Steady-state PL spectra were measured with a Horiba-Jobin Yvon Nanolog scanning spectrofluorometer equipped with a photomultiplier detector. Relative PL quantum yields (QYs) were measured following literature procedures, using either Rhodamine 590 or Rhodamine 640 dye as standard.[85] Absorption and PL emission spectra were measured as replicates of three or more and the average QYs were recorded.

PL Lifetime Measurements. Excited state lifetimes were measured with the time-correlated single-photon counting (TCSPC) technique. For $CH_3NH_3PbI_3$, a pulse diode laser from PicoQuant (model PDL 800-B) was used as an excitation source, providing a wavelength of 638 nm with a repetition rate of 5-MHz. A set of polarizers was incorporated with a magic angle (54.7°) arrangement. A photon counting module (Becker & Hickl model SPC-630) and appropriate filters were used to collect the PL. For $CH_3NH_3PbBr_3$, a similar system that uses a pulsed supercontinuum laser (SC-450-pp-he, Fianium, Southampton, U.K.) for the excitation was also employed. A small-band-pass filter centered at 500 nm was used to select excitation wavelength from the supercontinuum source that was pulsed at a repetition rate of 2-MHz. With the systems described, the full-width at half-maximum of the instrument response (IRF) was ∼200 ps. Generally, for lifetime experiments 30 000 counts were accumulated in the peak channel unless specified otherwise. A cuvette of 3 mm or 10 mm path length was used for the time-resolved measurement, depending on the sample. The decay parameters were determined by fitting to a sum of exponentials after deconvolution of instrument response function.

Single Particle Fluorescence Microscopy. Single particle fluorescence microscopy was performed using an inverted microscope operated in epi-fluorescence mode (Nikon Eclipse TE2000U Melville, NY). Perovskites were diluted in toluene and sonicated for 2 h before depositing 50 μL on a glass microscope coverslip (Carlson Scientific, Peotone, IL). After 3 min, the solution was removed under vacuum and the sample dried. A mercury lamp was used for excitation. A filter set from Omega Optical (Brattleboro, VT) was equipped with 540/20 nm excitation and 700/75 nm emission filter. The dichroic filter used was 560DRLP. A 100× Plan Apo, 1.49 numerical aperture oil-immersion objective was used for all experiments. Single-particle PL images were collected on a PhotonMAX 512 EMCCD camera (Princeton Instrument, Trenton, NJ) with 50 ms exposure time and no gain.

Each movie was 25 s in duration and 5 movies were collected per sample. ImageJ was used to analyze the PL intensity *versus* time for the background and selected particles.

Registered Atomic Force Microscopy-Photoluminescence-(AFM-PL). Sample coverslips were mounted on the stage of an inverted optical microscope (Olympus IX71) equipped with a piezoelectric scanner (Physik Instrumente P773.3CD XYZ) for positioning isolated wire or rod structures in the optical probe region of the microscope. Excitation was provided by a 485 nm pulsed diode laser (PicoQuant LDH-P-C 485B) operating at a pulse repetition rate of either 5 or 10 MHz and pulse width of ~100 ps. The laser light was focused onto the stage with a 1.4 NA/100× oil immersion microscope objective to form an approximately 0.5-μm-diameter optical probe region at the top surface of the coverslip. Average excitation powers were in the range of 2−10 nW. Emitted fluorescence was collected by the same microscope objective and directed onto a single-photon counting avalanche photodiode detector (APD) (PerkinElmer SPCM-14AQR). The emission was spatially filtered with a 75-μm-diameter pinhole located in the image plane of the microscope and spectrally filtered with a 160 nm bandpass filter centered at 791 nm (Semrock) before reaching the detector. For particularly bright structures, a neutral density (ND 1) filter was placed in front of the bandpass filter to attenuate the photoluminescence reaching the detector. The output of the APD was directed to a time-correlated single-photon counting photon counting module (PicoQuant PicoHarp 300) to record the photon data. The photon data were postprocessed with vendor-supplied software (Picoquant Symphotime) to obtain the photoluminescence images. An atomic force microscope (AFM) (Veeco Instruments Bioscope SZ), mounted on the stage of the inverted optical microscope, was used to record nanometer scale topography images of the rod and wire structures imaged by the optical microscope. The AFM height images were obtained using Si nanoprobes operated in tapping mode with resonance frequency of approximately 300 kHz. Spatial alignment of the AFM tip with the optical probe region was accomplished by monitoring the excitation laser light scattered from the tip with a second APD. Correlated photoluminescence and AFM height images were obtained by first raster scanning the sample through the optical probe volume to record the photoluminescence image and then engaging and raster scanning the AFM probe to record the AFM image from the stationary sample.

Conflict of Interest: The authors declare no competing financial interest.

Supporting Information Available: Reported XRD patterns for $(CH_3NH_3)_nPbI_m$ and $(CH_3NH_3)_nPbBr_m$ (n,m = 2,4; 3,5; 4,6), time-resolved photoluminescence data for $CH_3NH_3PbI_3$, single particle fluorescence microscopy movies and traces for $CH_3NH_3PbI_3$ (dots, wires, plates), additional e-beam instability data for $CH_3NH_3PbBr_3$, and IR and XRD *vs*TEM particle size comparison for $CH_3NH_3PbI_3$. This material is available free of charge *via* the Internet at http://pubs.acs.org.

Acknowledgment. This research is supported by the U.S. Department of Energy, Office of Basic Energy Sciences, Division of Chemical Sciences, Geosciences, and Biosciences through the Ames Laboratory. The Ames Laboratory is operated for the U.S. Department of Energy by Iowa State University under Contract No. DE-AC02-07CH11358. This work was performed, in part (AFM/PL), at the Center for Integrated Nanotechnologies, an Office of Science User Facility operated for the U.S. Department of Energy (DOE) Office of Science. Los Alamos National Laboratory, an affirmative action equal opportunity employer, is operated by Los Alamos National Security, LLC, for the National Nuclear Security Administration of the U.S. Department of Energy under contract DE-AC52-06NA25396.

REFERENCES AND NOTES

1. Snaith, H. J. Perovskites: The Emergence of a New Era for Low-Cost, High-Efficiency Solar Cells. *J. Phys. Chem. Lett.* **2013**, *4*, 3623–3630.
2. Kamat, P. V. Evolution of Perovskite Photovoltaics and Decrease in Energy Payback Time. *J. Phys. Chem. Lett.* **2013**, *4*, 3733–3734.
3. Bisquert, J. The Swift Surge of Perovskite Photovoltaics. *J. Phys. Chem. Lett.* **2013**, *4*, 2597–2598.
4. Park, N.-G. Organometal Perovskite Light Absorbers toward a 20% Efficiency Low-Cost Solid-State Mesoscopic Solar Cell. *J. Phys. Chem. Lett.* **2013**, *4*, 2423–2429.
5. Kazim, S.; Nazeeruddin, M. K.; Grätzel, M.; Ahmad, S. Perovskite as Light Harvester: A Game Changer in Photovoltaics. *Angew. Chem., Int. Ed.* **2014**, *53*, 2812–2824.
6. Liu, M.; Johnston, M. B.; Snaith, H. J. Efficient Planar Heterojunction Perovskite Solar Cells by Vapour Deposition. *Nature* **2013**, *501*, 395–398.
7. Gratzel, M. The Light and Shade of Perovskite Solar Cells. *Nat. Mater.* **2014**, *13*, 838–842.
8. Eperon, G. E.; Stranks, S. D.; Menelaou, C.; Johnston, M. B.; Herz, L. M.; Snaith, H. J. Formamidinium Lead Trihalide: A Broadly Tunable Perovskite for Efficient Planar Heterojunction Solar Cells. *Energy Environ. Sci.* **2014**, *7*, 982–988.
9. Pang, S.; Hu, H.; Zhang, J.; Lv, S.; Yu, Y.; Wei, F.; Qin, T.; Xu, H.; Liu, Z.; Cui, G. $NH_2CH{=}NH_2PbI_3$: An Alternative Organolead Iodide Perovskite Sensitizer for Mesoscopic Solar Cells. *Chem. Mater.* **2014**, *26*, 1485–1491.
10. Pellet, N.; Gao, P.; Gregori, G.; Yang, T.-Y.; Nazeeruddin, M. K.; Maier, J.; Grätzel, M. Mixed-Organic-Cation Perovskite Photovoltaics for Enhanced Solar-Light Harvesting. *Angew. Chem., Int. Ed.* **2014**, *53*, 3151–3157.
11. Ogomi, Y.; Morita, A.; Tsukamoto, S.; Saitho, T.; Fujikawa, N.; Shen, Q.; Toyoda, T.; Yoshino, K.; Pandey, S. S.; Ma, T.; et al. $CH_3NH_3Sn_xPb_{(1-x)}I_3$ Perovskite Solar Cells Covering up to 1060 nm. *J. Phys. Chem. Lett.* **2014**, *5*, 1004–1011.
12. Hao, F.; Stoumpos, C. C.; Chang, R. P. H.; Kanatzidis, M. G. Anomalous Band Gap Behavior in Mixed Sn and Pb Perovskites Enables Broadening of Absorption Spectrum in Solar Cells. *J. Am. Chem. Soc.* **2014**, *136*, 8094–8099.
13. Hao, F.; Stoumpos, C. C.; Cao, D. H.; Chang, R. P. H.; Kanatzidis, M. G. Lead-Free Solid-State Organic-Inorganic Halide Perovskite Solar Cells. *Nat. Photonics* **2014**, *8*, 489–494.
14. Noel, N. K.; Stranks, S. D.; Abate, A.; Wehrenfennig, C.; Guarnera, S.; Haghighirad, A.; Sadhanala, A.; Eperon, G. E.; Pathak, S. K.; Johnston, M. B.; et al. Lead-Free Organic-Inorganic Tin Halide Perovskites for Photovoltaic Applications. *Energy Environ. Sci.* **2014**, *7*, 3061–3068.
15. Edri, E.; Kirmayer, S.; Cahen, D.; Hodes, G. High Open-Circuit Voltage Solar Cells Based on Organic−Inorganic Lead Bromide Perovskite. *J. Phys. Chem. Lett.* **2013**, *4*, 897–902.
16. Stoumpos, C. C.; Malliakas, C. D.; Kanatzidis, M. G. Semiconducting Tin and Lead Iodide Perovskites with Organic Cations: Phase Transitions, High Mobilities, and Near-Infrared Photoluminescent Properties. *Inorg. Chem.* **2013**, *52*, 9019–9038.
17. Stranks, S. D.; Eperon, G. E.; Grancini, G.; Menelaou, C.; Alcocer, M. J. P.; Leijtens, T.; Herz, L. M.; Petrozza, A.; Snaith, H. J. Electron-Hole Diffusion Lengths Exceeding 1 Micrometer in an Organometal Trihalide Perovskite Absorber. *Science* **2013**, *342*, 341–344.
18. Kim, H.-S.; Lee, C.-R.; Im, J.-H.; Lee, K.-B.; Moehl, T.; Marchioro, A.; Moon, S.-J.; Humphry-Baker, R.; Yum, J.-H.; Moser, J. E.; Gratzel, M.; Park, N.-G. Lead Iodide Perovskite Sensitized All-Solid-State Submicron Thin Film Mesoscopic Solar Cell with Efficiency Exceeding 9%. *Sci. Rep.* **2012**, *2*, 591.
19. Kojima, A.; Teshima, K.; Shirai, Y.; Miyasaka, T. Organometal Halide Perovskites as Visible-Light Sensitizers for Photovoltaic Cells. *J. Am. Chem. Soc.* **2009**, *131*, 6050–6051.
20. Service, R. F. Perovskite Solar Cells Keep On Surging. *Science* **2014**, *344*, 458.
21. Choi, J. J.; Yang, X.; Norman, Z. M.; Billinge, S. J. L.; Owen, J. S. Structure of Methylammonium Lead Iodide within Mesoporous Titanium Dioxide: Active Material in High-Performance Perovskite Solar Cells. *Nano Lett.* **2013**, *14*, 127–133.

22. Dualeh, A.; Tétreault, N.; Moehl, T.; Gao, P.; Nazeeruddin, M. K.; Grätzel, M. Effect of Annealing Temperature on Film Morphology of Organic–Inorganic Hybrid Pervoskite Solid-State Solar Cells. *Adv. Funct. Mater.* **2014**, *24*, 3250–3258.
23. Tan, K. W.; Moore, D. T.; Saliba, M.; Sai, H.; Estroff, L. A.; Hanrath, T.; Snaith, H. J.; Wiesner, U. Thermally Induced Structural Evolution and Performance of Mesoporous Block Copolymer-Directed Alumina Perovskite Solar Cells. *ACS Nano* **2014**, *8*, 4730–4739.
24. Eperon, G. E.; Burlakov, V. M.; Docampo, P.; Goriely, A.; Snaith, H. J. Morphological Control for High Performance, Solution-Processed Planar Heterojunction Perovskite Solar Cells. *Adv. Funct. Mater.* **2013**, *24*, 151–157.
25. Burlakov, V. M.; Eperon, G. E.; Snaith, H. J.; Chapman, S. J.; Goriely, A. Controlling Coverage of Solution Cast Materials with Unfavourable Surface Interactions. *Appl. Phys. Lett.* **2014**, *104*, 091602.
26. Liang, P.-W.; Liao, C.-Y.; Chueh, C.-C.; Zuo, F.; Williams, S. T.; Xin, X.-K.; Lin, J.; Jen, A. K. Y. Additive Enhanced Crystallization of Solution-Processed Perovskite for Highly Efficient Planar-Heterojunction Solar Cells. *Adv. Mater.* **2014**, *26*, 3748–3754.
27. Saliba, M.; Tan, K. W.; Sai, H.; Moore, D. T.; Scott, T.; Zhang, W.; Estroff, L. A.; Wiesner, U.; Snaith, H. J. Influence of Thermal Processing Protocol upon the Crystallization and Photovoltaic Performance of Organic–Inorganic Lead Trihalide Perovskites. *J. Phys. Chem. C* **2014**, *118*, 17171–17177.
28. Zhao, Y.; Zhu, K. CH_3NH_3Cl-Assisted One-Step Solution Growth of $CH_3NH_3PbI_3$: Structure, Charge-Carrier Dynamics, and Photovoltaic Properties of Perovskite Solar Cells. *J. Phys. Chem. C* **2014**, *118*, 9412–9418.
29. Chen, Q.; Zhou, H.; Hong, Z.; Luo, S.; Duan, H.-S.; Wang, H.-H.; Liu, Y.; Li, G.; Yang, Y. Planar Heterojunction Perovskite Solar Cells *via* Vapor-Assisted Solution Process. *J. Am. Chem. Soc.* **2013**, *136*, 622–625.
30. Heo, J. H.; Song, D. H.; Im, S. H. Planar $CH_3NH_3PbBr_3$ Hybrid Solar Cells with 10.4% Power Conversion Efficiency, Fabricated by Controlled Crystallization in the Spin-Coating Process. *Adv. Mater.* **2014**, *26*, 8179–8183.
31. Kang, R.; Kim, J.-E.; Yeo, J.-S.; Lee, S.; Jeon, Y.-j.; Kim, D.-Y. Optimized Organometal Halide Perovskite Planar Hybrid Solar Cells *via* Control of Solvent Evaporation Rate. *J. Phys. Chem. C* **2014**, *118*, 26513–26520.
32. Jeon, N. J.; Noh, J. H.; Kim, Y. C.; Yang, W. S.; Ryu, S.; Seok, S. I. Solvent Engineering for High-Performance Inorganic–Organic Hybrid Perovskite Solar Cells. *Nat. Mater.* **2014**, *13*, 897–903.
33. Burschka, J.; Pellet, N.; Moon, S.-J.; Humphry-Baker, R.; Gao, P.; Nazeeruddin, M. K.; Graetzel, M. Sequential Deposition as a Route to High-Performance Perovskite-Sensitized Solar Cells. *Nature* **2013**, *499*, 316–319.
34. Kulkarni, S. A.; Baikie, T.; Boix, P. P.; Yantara, N.; Mathews, N.; Mhaisalkar, S. G. Band Gap Tuning of Lead Halide Perovskites Using a Sequential Deposition Process. *J. Mater. Chem. A* **2014**, *2*, 9221–9225.
35. Shi, J.; Luo, Y.; Wei, H.; Luo, J.; Dong, J.; Lv, S.; Xiao, J.; Xu, Y.; Zhu, L.; Xu, X.; et al. Modified Two-Step Deposition Method for High-Efficiency $TiO_2/CH_3NH_3PbI_3$ Heterojunction Solar Cells. *ACS Appl. Mater. Interfaces* **2014**, *6*, 9711–9718.
36. Liu, D.; Kelly, T. L. Perovskite Solar Cells with a Planar Heterojunction Structure Prepared Using Room-Temperature Solution Processing Techniques. *Nat. Photonics* **2014**, *8*, 133–138.
37. Bi, D.; El-Zohry, A. M.; Hagfeldt, A.; Boschloo, G. Improved Morphology Control Using a Modified Two-Step Method for Efficient Perovskite Solar Cells. *ACS Appl. Mater. Interfaces* **2014**, *6*, 18751–18757.
38. Im, J.-H.; Jang, I.-H.; Pellet, N.; Grätzel, M.; Park, N.-G. Growth of $CH_3NH_3PbI_3$ Cuboids with Controlled Size for High-Efficiency Perovskite Solar Cells. *Nat. Nanotechnol.* **2014**, *9*, 927–932.
39. Shkrob, I. A.; Marin, T. W. Charge Trapping in Photovoltaically Active Perovskites and Related Halogenoplumbate Compounds. *J. Phys. Chem. Lett.* **2014**, *5*, 1066–1071.
40. Snaith, H. J.; Abate, A.; Ball, J. M.; Eperon, G. E.; Leijtens, T.; Noel, N. K.; Stranks, S. D.; Wang, J. T.-W.; Wojciechowski, K.; Zhang, W. Anomalous Hysteresis in Perovskite Solar Cells. *J. Phys. Chem. Lett.* **2014**, *5*, 1511–1515.
41. Abate, A.; Saliba, M.; Hollman, D. J.; Stranks, S. D.; Wojciechowski, K.; Avolio, R.; Grancini, G.; Petrozza, A.; Snaith, H. J. Supramolecular Halogen Bond Passivation of Organic–Inorganic Halide Perovskite Solar Cells. *Nano Lett.* **2014**, *14*, 3247–3254.
42. Schmidt, L. C.; Pertegás, A.; González-Carrero, S.; Malinkiewicz, O.; Agouram, S.; Mínguez Espallargas, G.; Bolink, H. J.; Galian, R. E.; Pérez-Prieto, J. Nontemplate Synthesis of $CH_3NH_3PbBr_3$ Perovskite Nanoparticles. *J. Am. Chem. Soc.* **2014**, *9*, 927–932.
43. Wehrenfennig, C.; Liu, M.; Snaith, H. J.; Johnston, M. B.; Herz, L. M. Homogeneous Emission Line Broadening in the Organo Lead Halide Perovskite $CH_3NH_3PbI_{3-x}Cl_x$. *J. Phys. Chem. Lett.* **2014**, *5*, 1300–1306.
44. Deschler, F.; Price, M.; Pathak, S.; Klintberg, L. E.; Jarausch, D.-D.; Higler, R.; Hüttner, S.; Leijtens, T.; Stranks, S. D.; Snaith, H. J.; et al. High Photoluminescence Efficiency and Optically Pumped Lasing in Solution-Processed Mixed Halide Perovskite Semiconductors. *J. Phys. Chem. Lett.* **2014**, *5*, 1421–1426.
45. Ha, S. T.; Liu, X.; Zhang, Q.; Giovanni, D.; Sum, T. C.; Xiong, Q. Synthesis of Organic–Inorganic Lead Halide Perovskite Nanoplatelets: Towards High-Performance Perovskite Solar Cells and Optoelectronic Devices. *Adv. Opt. Mater.* **2014**, *2*, 838–844.
46. Zhenhua, C.; Hui, L.; Yongbing, T.; Xing, H.; Derek, H.; Chun-Sing, L. Shape-Controlled Synthesis of Organolead Halide Perovskite Nanocrystals and their Tunable Optical Absorption. *Mater. Res. Express* **2014**, *1*, 015034.
47. Yang, S.; Zheng, Y. C.; Hou, Y.; Chen, X.; Chen, Y.; Wang, Y.; Zhao, H.; Yang, H. G. Formation Mechanism of Freestanding $CH_3NH_3PbI_3$ Functional Crystals: *In Situ* Transformation *vs* Dissolution–Crystallization. *Chem. Mater.* **2014**, *26*, 6705–6710.
48. Payne, R. Incidence of Humps in the Double-Layer Capacity at the Mercury-Nonaqueous Solution Interface. *J. Phys. Chem.* **1967**, *71*, 1548–1549.
49. Mitzi, D. B. Templating and Structural Engineering in Organic-Inorganic Perovskites. *J. Chem. Soc., Dalton Trans.* **2001**, 1–12.
50. Mitzi, D. B. Solution-Processed Inorganic Semiconductors. *J. Mater. Chem.* **2004**, *14*, 2355–2365.
51. Mitzi, D. B.; Liang, K. Synthesis, Resistivity, and Thermal Properties of the Cubic Perovskite $NH_2CH{=}NH_2SnI_3$ and Related Systems. *J. Solid State Chem.* **1997**, *134*, 376–381.
52. Mosconi, E.; Amat, A.; Nazeeruddin, M. K.; Grätzel, M.; De Angelis, F. First-Principles Modeling of Mixed Halide Organometal Perovskites for Photovoltaic Applications. *J. Phys. Chem. C* **2013**, *117*, 13902–13913.
53. Huang, L.-Y.; Lambrecht, W. R. L. Electronic Band Structure, Phonons, and Exciton Binding Energies of Halide Perovskites $CsSnCl_3$, $CsSnBr_3$, and $CsSnI_3$. *Phys. Rev. B* **2013**, *88*, 165203.
54. Im, J.-H.; Chung, J.; Kim, S.-J.; Park, N.-G. Synthesis, Structure, and Photovoltaic Property of a Nanocrystalline 2H Perovskite-Type Novel Sensitizer $(CH_3CH_2NH_3)PbI_3$. *Nanoscale Res. Lett.* **2012**, *7*, 353.
55. Amat, A.; Mosconi, E.; Ronca, E.; Quarti, C.; Umari, P.; Nazeeruddin, M. K.; Grätzel, M.; De Angelis, F. Cation-Induced Band-Gap Tuning in Organohalide Perovskites: Interplay of Spin–Orbit Coupling and Octahedra Tilting. *Nano Lett.* **2014**, *14*, 3608–3616.
56. Edri, E.; Kirmayer, S.; Kulbak, M.; Hodes, G.; Cahen, D. Chloride Inclusion and Hole Transport Material Doping to Improve Methyl Ammonium Lead Bromide Perovskite-Based High Open-Circuit Voltage Solar Cells. *J. Phys. Chem. Lett.* **2014**, *5*, 429–433.
57. Colella, S.; Mosconi, E.; Fedeli, P.; Listorti, A.; Gazza, F.; Orlandi, F.; Ferro, P.; Besagni, T.; Rizzo, A.; Calestani, G.; et al. $MAPbI_{3-x}Clx$ Mixed Halide Perovskite for Hybrid Solar Cells:

The Role of Chloride as Dopant on the Transport and Structural Properties. *Chem. Mater.* **2013**, *25*, 4613–4618.
58. Noh, J. H.; Im, S. H.; Heo, J. H.; Mandal, T. N.; Seok, S. I. Chemical Management for Colorful, Efficient, and Stable Inorganic–Organic Hybrid Nanostructured Solar Cells. *Nano Lett.* **2013**, *13*, 1764–1769.
59. Poglitsch, A.; Weber, D. Dynamic Disorder in Methylammoniumtrihalogenoplumbates(II) Observed by Millimeter-Wave Spectroscopy. *J. Chem. Phys.* **1987**, *87*, 6373–6378.
60. Dualeh, A.; Gao, P.; Seok, S. I.; Nazeeruddin, M. K.; Grätzel, M. Thermal Behavior of Methylammonium Lead-Trihalide Perovskite Photovoltaic Light Harvesters. *Chem. Mater.* **2014**, *26*, 6160–6164.
61. Tanaka, K.; Takahashi, T.; Ban, T.; Kondo, T.; Uchida, K.; Miura, N. Comparative Study on the Excitons in Lead-Halide-Based Perovskite-Type Crystals $CH_3NH_3PbBr_3$ $CH_3NH_3PbI_3$. *Solid State Commun.* **2003**, *127*, 619–623.
62. D'Innocenzo, V.; Kandada, A. R. S.; De Bastiani, M.; Gandini, M.; Petrozza, A. Tuning the Light Emission Properties by Band Gap Engineering in Hybrid Lead Halide Perovskite. *J. Am. Chem. Soc.* **2014**, *136*, 17730–17733.
63. Schnitzer, I.; Yablonovitch, E.; Caneau, C.; Gmitter, T. J. Ultrahigh Spontaneous Emission Quantum Efficiency, 99.7% Internally and 72% Externally, from AlGaAs/GaAs/AlGaAs Double Heterostructures. *Appl. Phys. Lett.* **1993**, *62*, 131–133.
64. Barkhouse, D. A. R.; Pattantyus-Abraham, A. G.; Levina, L.; Sargent, E. H. Thiols Passivate Recombination Centers in Colloidal Quantum Dots Leading to Enhanced Photovoltaic Device Efficiency. *ACS Nano* **2008**, *2*, 2356–2362.
65. Kim, J.; Lee, S.-H.; Lee, J. H.; Hong, K.-H. The Role of Intrinsic Defects in Methylammonium Lead Iodide Perovskite. *J. Phys. Chem. Lett.* **2014**, *5*, 1312–1317.
66. Buin, A.; Pietsch, P.; Xu, J.; Voznyy, O.; Ip, A. H.; Comin, R.; Sargent, E. H. Materials Processing Routes to Trap-Free Halide Perovskites. *Nano Lett.* **2014**, *14*, 6281–6286.
67. Glennon, J. J.; Tang, R.; Buhro, W. E.; Loomis, R. A. Synchronous Photoluminescence Intermittency (Blinking) along Whole Semiconductor Quantum Wires. *Nano Lett.* **2007**, *7*, 3290–3295.
68. Wang, S.; Querner, C.; Emmons, T.; Drndic, M.; Crouch, C. H. Fluorescence Blinking Statistics from CdSe Core and Core/Shell Nanorods. *J. Phys. Chem. B* **2006**, *110*, 23221–23227.
69. Protasenko, V. V.; Hull, K. L.; Kuno, M. Disorder-Induced Optical Heterogeneity in Single CdSe Nanowires. *Adv. Mater.* **2005**, *17*, 2942–2949.
70. Rothenberg, E.; Ebenstein, Y.; Kazes, M.; Banin, U. Two-Photon Fluorescence Microscopy of Single Semiconductor Quantum Rods: Direct Observation of Highly Polarized Nonlinear Absorption Dipole. *J. Phys. Chem. B* **2004**, *108*, 2797–2800.
71. Rothenberg, E.; Kazes, M.; Shaviv, E.; Banin, U. Electric Field Induced Switching of the Fluorescence of Single Semiconductor Quantum Rods. *Nano Lett.* **2005**, *5*, 1581–1586.
72. Titova, L. V.; Hoang, T. B.; Jackson, H. E.; Smith, L. M.; Yarrison-Rice, J. M.; Lensch, J. L.; Lauhon, L. J. Low-Temperature Photoluminescence Imaging and Time-Resolved Spectroscopy of Single CdS Nanowires. *Appl. Phys. Lett.* **2006**, *89*, 053119.
73. Glennon, J. J.; Buhro, W. E.; Loomis, R. A. Simple Surface-Trap-Filling Model for Photoluminescence Blinking Spanning Entire CdSe Quantum Wires. *J. Phys. Chem. C* **2008**, *112*, 4813–4817.
74. Sköld, N.; Karlsson, L. S.; Larsson, M. W.; Pistol, M.-E.; Seifert, W.; Trägårdh, J.; Samuelson, L. Growth and Optical Properties of Strained GaAs–$Ga_xIn_{1-x}P$ Core–Shell Nanowires. *Nano Lett.* **2005**, *5*, 1943–1947.
75. Gudiksen, M. S.; Wang, J.; Lieber, C. M. Size-Dependent Photoluminescence from Single Indium Phosphide Nanowires. *J. Phys. Chem. B* **2002**, *106*, 4036–4039.
76. Hua, B.; Motohisa, J.; Kobayashi, Y.; Hara, S.; Fukui, T. Single GaAs/GaAsP Coaxial Core–Shell Nanowire Lasers. *Nano Lett.* **2008**, *9*, 112–116.
77. Agarwal, R.; Barrelet, C. J.; Lieber, C. M. Lasing in Single Cadmium Sulfide Nanowire Optical Cavities. *Nano Lett.* **2005**, *5*, 917–920.
78. Tang, Z.; Kotov, N. A.; Giersig, M. Spontaneous Organization of Single CdTe Nanoparticles into Luminescent Nanowires. *Science* **2002**, *297*, 237–240.
79. Titova, L. V.; Hoang, T. B.; Jackson, H. E.; Smith, L. M.; Yarrison-Rice, J. M.; Kim, Y.; Joyce, H. J.; Tan, H. H.; Jagadish, C. Temperature Dependence of Photoluminescence from Single Core-Shell GaAs-AlGaAs Nanowires. *Appl. Phys. Lett.* **2006**, *89*, 173126–1–173126–3.
80. Wang, J.; Gudiksen, M. S.; Duan, X.; Cui, Y.; Lieber, C. M. Highly Polarized Photoluminescence and Photodetection from Single Indium Phosphide Nanowires. *Science* **2001**, *293*, 1455–1457.
81. Wayman, V. L.; Morrison, P. J.; Wang, F.; Tang, R.; Buhro, W. E.; Loomis, R. A. Bound 1D Excitons in Single CdSe Quantum Wires. *J. Phys. Chem. Lett.* **2012**, *3*, 2627–2632.
82. Glennon, J. J.; Tang, R.; Buhro, W. E.; Loomis, R. A.; Bussian, D. A.; Htoon, H.; Klimov, V. I. Exciton Localization and Migration in Individual CdSe Quantum Wires at Low Temperatures. *Phys. Rev. B* **2009**, *80*, 081303.
83. Böhmler, M.; Wang, Z.; Myalitsin, A.; Mews, A.; Hartschuh, A. Optical Imaging of CdSe Nanowires with Nanoscale Resolution. *Angew. Chem., Int. Ed.* **2011**, *50*, 11536–11538.
84. Lee, M. M.; Teuscher, J.; Miyasaka, T.; Murakami, T. N.; Snaith, H. J. Efficient Hybrid Solar Cells Based on Meso-Superstructured Organometal Halide Perovskites. *Science* **2012**, *338*, 643–647.
85. Grabolle, M.; Spieles, M.; Lesnyak, V.; Gaponik, N.; Eychmüller, A.; Resch-Genger, U. Determination of the Fluorescence Quantum Yield of Quantum Dots: Suitable Procedures and Achievable Uncertainties. *Anal. Chem.* **2009**, *81*, 6285–6294.